clean technologies

MDPI

Article

Nitrogen-Doped Calcite Derived from Ca-MOFs as an Efficient Adsorbent for Sr(II) Removal from Water: The Role of Nitrogen and Calcium

Xinran Xie [1,2], Guoce Yu [1,*], Jiangbo Huo [2,3,*], Xinbo Zhang [2,3] and Qing Du [2,3]

[1] Laboratory of Environmental Technology, INET, Tsinghua University, Beijing 100084, China; 15531675157@139.com
[2] Joint Research Centre for Protective Infrastructure Technology and Environmental Green Bioprocess, School of Environmental and Municipal Engineering, Tianjin Chengjian University, Tianjin 300384, China; zxbcj2006@126.com (X.Z.); duqing1@tcu.edu.cn (Q.D.)
[3] Tianjin Key Laboratory of Aquatic Science and Technology, Tianjin Chengjian University, Jinjing Road 26, Tianjin 300384, China
* Correspondence: yugc@tsinghua.edu.cn (G.Y.); huozhaoyuan@163.com (J.H.)

Abstract: Strontium (^{90}Sr) is a typical radionuclide, which can act as a contaminant and poses a big problem for the eco-environment if left untreated. In this study, an original nitrogen-doped calcite (N-$CaCO_3$) was synthesized using a solvothermal and calcination method and used to remove Sr(II) from simulated water. XRD, SEM, and XPS analyses proved that N was successfully doped into $CaCO_3$, resulting in porous $CaCO_3$ with a regular morphology. The specific surface area of N-$CaCO_3$ (136.53 m^2/g) can reach 2.19-fold greater than that of $CaCO_3$. The results based on the batch adsorption data indicated that the pseudo-second-order kinetic model (R^2 = 0.9964) and the ion exchange model (R^2 = 0.9859) fitted the adsorption data well. The as-synthesized N-$CaCO_3$ exhibited better adsorption performance in regard to low concentrations of Sr(II) (below 64.5 mg/L) compared with commercial $CaCO_3$. The structural analysis suggested that Ca and N played pivotal roles in the adsorption process and that the adsorption mechanism was dominated by ion exchange and surface complexation. This study successfully fabricated a nitrogen-doped calcite for Sr(II) cleanup, presenting an efficient strategy to modulate the microstructure of $CaCO_3$, or other materials, to enhance its adsorption performance.

Keywords: nitrogen calcite; Sr(II); Ca-MOFs; adsorption; radioactive wastewater

Academic Editor: Alírio E. Rodrigues

Received: 30 November 2024
Revised: 24 December 2024
Accepted: 26 December 2024
Published: 27 December 2024

Citation: Xie, X.; Yu, G.; Huo, J.; Zhang, X.; Du, Q. Nitrogen-Doped Calcite Derived from Ca-MOFs as an Efficient Adsorbent for Sr(II) Removal from Water: The Role of Nitrogen and Calcium. *Clean Technol.* **2025**, *7*, 2. https://doi.org/10.3390/cleantechnol7010002

1. Introduction

Nuclear energy has garnered significant attention and is regarded as one of the clean energy sources, which holds great promise in regard to sustainable development. However, the rapid expansion of nuclear power plants has caused severe environmental problems and health risks. During the application process involving nuclear technology, a substantial amount of radioactive isotopes is inevitably released into the environment. The removal and recovery of radionuclides from aqueous waste is of paramount importance [1,2]. In particular, the strontium isotope ^{90}Sr is a fission product from nuclear fuel (^{235}U) [3], which is difficult to capture from radioactive wastewater because of its high solubility, its high level of environmental mobility, its high level of radioactive toxicity, and its long half-life (28.78 years) [4]. Strontium has similar chemical properties to calcium and it can replace calcium in animal bones [5]. The deposition of ^{90}Sr in human bones can cause serious

health problems, including bone cancer, rickets, and leukemia [6]. Therefore, removing ^{90}Sr and reducing the risks posed has received widespread attention [7].

There are currently numerous methods for removing nuclides, such as chemical precipitation [8], electrochemical treatment [9], ion exchange [10], membrane treatment [11], biological treatment [12], and adsorption [13,14]. Among them, adsorption is always deemed to be one of the most popular methods because of its advantages, namely its simple operation [15], the wide range of possible sources of adsorbents, its low cost, and its considerable effectiveness. Many adsorbents have been reported for removing nuclides, which mainly includes carbon-based materials [16,17], clay-based adsorbents [18,19], metal oxides [20,21], and emerging coordination compounds, such as metal–organic frameworks [22–24].

Metal–organic frameworks (MOFs) are a novel class of crystalline materials, composed of metal ions (or metal clusters) and organic ligands (or small organic molecules). MOFs exhibit numerous distinct advantages in the field of adsorption. In regard to the structure of MOFs, metal ions are generally considered as nodes and organic polyanions (such as carboxylates, sulfonates, and phosphonates) as bridging linkers [25]. Among the linkers involved, aromatic carboxylate anions are particularly noteworthy due to their rigid organic skeleton and strong coordination capabilities in regard to many metals [26,27]. MOFs have characteristics including diverse topological structures, good chemical stability and thermal stability, easy functionalization, and a large specific surface area, etc. [28,29]. Highly porous MOFs have enough pore spaces and a strong ability to capture a wide range of metal ions, oxyanions, and organic pollutants [30–32]. For example, a Zn-based metal–organic framework was modified by $CuCl_2$ for the removal of Pb and Cd ions, and it showed satisfactory adsorption capacity for lead and cadmium (434.7 and 181.81 mg/g, respectively) [33]. Moreover, ^{137}Cs was removed using SZ-6 (a two-dimensional layered an–ion framework material) from an aqueous solution, which is currently one of the fastest adsorbents for Cs^+ removal [34]. Recent research highlights that the unique properties of MOFs have established them as an ideal foundation for investigating the adsorption mechanisms of specific substances. However, MOF-based materials show some limitations in regard to their application. Most MOFs are made of heavy metals, such as Fe, Cr, Mn, Zn, and Cu [35–37], which may cause secondary pollution. Green MOFs have garnered significant attention in the field of water treatment. Recently, calcium has emerged as a promising candidate in regard to the heavy metal components in MOFs, owing to its abundant availability on earth and its favorable biocompatibility, and Ca-MOFs have the potential to effectively address secondary pollution during water treatment. However, due to their compact microstructure, Ca-MOFs usually have a limited number of pores and poor adsorption performance. MOF derivatives not only have higher thermal and chemical stability than MOFs, but also have a unique pore structure that provides more active sites. It is thus crucial to manage the adjustment of the structure of Ca-MOFs to improve their adsorption capabilities [38]. Recently, Lauchnor et al. investigated $CaCO_3$ precipitation and strontium co-precipitation in a two-dimensional reactor involving a porous medium using the diuretic effect of Bacillus subtilis, and this method was found to precipitate 71−85% of the calcium and 59% of the strontium present [39]. Li et al. synthesized a layered calcium potassium phosphate material, which demonstrated fast uptake (94.1% Sr^{2+} in 120 min and 96.6% Co^{2+} in 10 min) and remarkable adsorption capacity (384 mg/g for Sr^{2+} and 382 mg/g for Co^{2+}) [40]. Commercial $CaCO_3$ has a compact structure that inhibits the release of Ca^{2+} and ion exchange with Sr(II) in water. Previous research has suggested that incorporating non-metallic elements into $CaCO_3$ could modify its microstructure, improving its mass transfer capability and enhancing its adsorption performance [40]. Taking inspiration from this research, we synthesized nitrogen-doped calcite (N-$CaCO_3$) from Ca-MOFs for enhanced Sr(II) cleanup.

In this work, we synthesized Ca-MOFs with different ligands and acquired N-$CaCO_3$ as one of the derivatives after calcination, and investigated the removal efficiency in regard to Sr(II), and explored the effects of nitrogen doping on the dense microstructure of $CaCO_3$. The structures of the materials were analyzed using XRD, SEM, XPS, BET, FTIR, EDS, and TG. The adsorption kinetics and isotherms, the effects of the dosage, the initial concentrations, and pH, as well as the adsorption mechanisms, were investigated. We found that the adsorption performance of N-$CaCO_3$-500-2 was much better than that of commercial $CaCO_3$ in regard to Sr(II). The results clearly prove that N-doping effectively modulated the dense structure of $CaCO_3$. N-$CaCO_3$ is a highly effective and environmentally friendly adsorbent for capturing radioactive isotopes. The adjustability of its surface properties and porous structure would enable this nanomaterial to be suitable for a wide range of applications [39].

2. Experimental Section

2.1. Chemicals

Hexahydrate strontium chloride ($SrCl_2 \cdot 6H_2O$) was obtained from Shantou Xilong Chemical Plant Co., Ltd., Shantou, Guangdong, China. Diamino-terephthalic acid (NH_2-H_2BDC, 98% purity) was purchased from Shandong Keyuan Biochemical Co., Ltd., Heze, Shandong, China. Dihydrate calcium chloride ($CaCl_2 \cdot 2H_2O$) and calcium carbonate ($CaCO_3$, 99% purity) were bought from Chengdu Cologne Chemical Co., Ltd., Chengdu, Sichuan, China and Shanghai Macklin Biochemical Co., Ltd., Shanghai, China, respectively. N,N-dimethylformamide (C_3H_7NO, DMF, 99.5% purity) and ethanol were purchased from Shanghai Boer Chemical Reagent Co., Ltd., Shanghai, China and Beijing Tongguang Fine Chemical Co., Ltd., Beijing, China, respectively. The strontium standard solution was obtained from the National Nonferrous Metals and Electronic Materials Analysis and Testing Center. All the reagents were of analytical grade and were used directly without purification.

2.2. Synthesis of Ca-MOFs and Derivatives

2.2.1. Synthesis of Ca-MOFs

In regard to the typical procedure, 2 mmol of the ligand (H_2BDC) and 2 mmol of $CaCl_2 \cdot 2H_2O$ were dissolved in a mixture of 35 mL DMF, 10 mL ethanol, and 5 mL H_2O. The solution was stirred magnetically for 20 min at room temperature. The obtained mixture was transferred to a reaction vessel and heated in an oven at 90 °C for 24 h. Powders were collected as a result of centrifugation and washed with DMF 4 times until the eluent of the material reached pH = 7. Ultimately, the Ca-MOF was obtained after drying in an oven at 70 °C for 12 h. (Similarly, Ca-MOF-NH_2 was synthesized with NH_2-H_2BDC, which was used as the ligand.)

2.2.2. Synthesis of $CaCO_3$-y-z and N-$CaCO_3$-y-z

The Ca-MOF was treated at y temperature (y = 300, 400, 500, 600, 700 °C) in an air atmosphere, at a heating rate of 10 °C/min, and held for z time (z = 2, 4, 6, 8 h) to obtain $CaCO_3$-y-z. The obtained $CaCO_3$-y-z was used for subsequent experiments after grinding. N-$CaCO_3$-y-z was synthesized in the same way as Ca-MOF-NH_2.

2.3. Characterization

The morphology of the materials was observed using a field emission scanning electronic microscope (SEM, Zeiss Sigma 300, Oberkochen, Germany). The element species were analyzed using Energy Dispersive Elemental Analysis (EDS). X-ray diffraction (XRD) was performed using a Rigaku ULTIMA IVXRD X-ray powder diffractometer in conditions

ranging from 0 to 70° in regard to an angle of 2θ. Fourier transform infrared spectroscopy (FT-IR) was used to record the total reflection via an infrared spectrometer (Brooke TENSOR27, Billerica, MA, USA). The specific surface area and pore size distribution of the nanomaterials were measured using a fully automatic specific surface area and pore size tester at 150 °C after 6 h of degassing (BET, McASAP 2460/2020, Norcross, GA, USA). X-ray photoelectron spectroscopy (XPS) measurements were taken using a Thermo Fisher Scientific K-Alpha XPS spectrometer. The Sr concentrations in the solution before and after adsorption were quantitatively determined using an atomic absorption spectrophotometer (HITACHI ZA3000, Tokyo, Japan).

2.4. Adsorption Experiment

All the adsorption experiments were conducted in duplicate, under the same conditions. The adsorption experiments were conducted in a 50 mL centrifuge tube containing 60 mg of the adsorbent and 20 mL of the different solutions, with an initial Sr(II) concentration of 5 mg·L^{-1}. The mixture was placed in an incubator and shaken at a speed of 200 rpm at different operating temperatures. The concentration of Sr(II) in the solution was measured using an atomic absorption spectrometer at a wavelength of 460.7 nm. The adsorption efficiency R (%) of the adsorbent for Sr(II) was calculated using the following equation:

$$R(\%) = \frac{C_0 - C_t}{C_0} \times 100\% \quad (1)$$

where C_0 (mg·L^{-1}) and C_t (mg·L^{-1}) are the initial concentration and the concentration at time t of Sr(II), respectively.

The effect of pH on the removal of Sr(II) was investigated and the pH of the Sr(II) solution was adjusted by adding appropriate amounts of 0.1 mol/L NaOH or HCl solution. Subsequently, 60 mg of the adsorbent was dispersed in 20 mL of the Sr(II) solution, which had been adjusted to the desired pH. The prepared mixtures were then sealed and stirred at 25 °C for 24 h.

Adsorption isotherm and kinetic tests were conducted at 25 °C and pH 7. In regard to the adsorption isotherm test, 60 mg of N-$CaCO_3$-500-2 and 60 mg of commercial $CaCO_3$ were each added to 20 mL of the Sr(II) solution, with the concentration ranging from 3 mg/L to 120 mg/L. The mixtures were then shaken for a duration of 24 h.

3. Results

3.1. Structural Analysis

As presented in Figure 1a,b, the SEM images showed the structural appearance of Ca-MOF and Ca-MOF-NH_2. Ca-MOF exhibited a uniform layered structure, whereas Ca-MOF-NH_2 displayed a clustered block-like structure. After calcination, Figure 1c reveals that Ca-MOF experienced a reduction in particle size and an increase in surface roughness, resulting in significant changes to its porosity, similar to previous research findings [41]. Figure 1d indicates that N-$CaCO_3$-500-2 had a porous morphology, with an ordered and compact arrangement after calcination. This suggests that the doping of nitrogen atoms significantly affected the combination method, leading to the formation of two distinctive types of Ca-MOF derivatives. The porous texture may further facilitate surface adsorption in water [26].

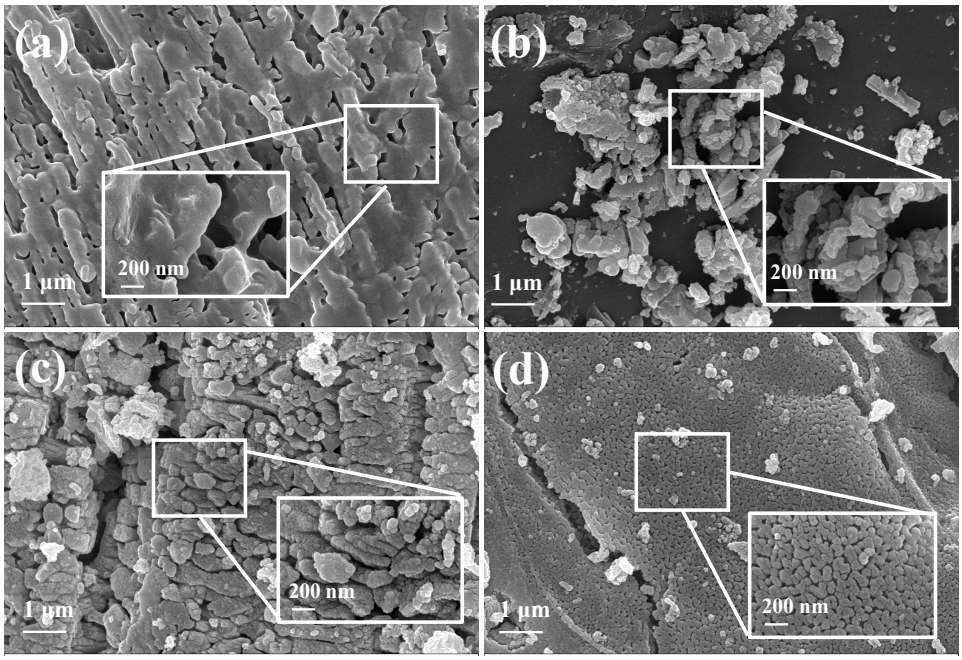

Figure 1. SEM images of (**a**) Ca-MOF, (**b**) Ca-MOF-NH_2, (**c**) $CaCO_3$-500-2, (**d**) N-$CaCO_3$-500-2.

The XRD patterns (Figure 2a) indicated that N-$CaCO_3$-500-2 was crystalline, with a rhombohedral crystal structure. The diffraction peaks of the N-$CaCO_3$-500-2 derivative were similar to those of the $CaCO_3$ sample (PDF#: No. 00-005-0586), with peaks located at 2θ = 29.41°, 39.40°, 47.49°, and 48.51°, which clearly confirmed that the calcination product was $CaCO_3$.

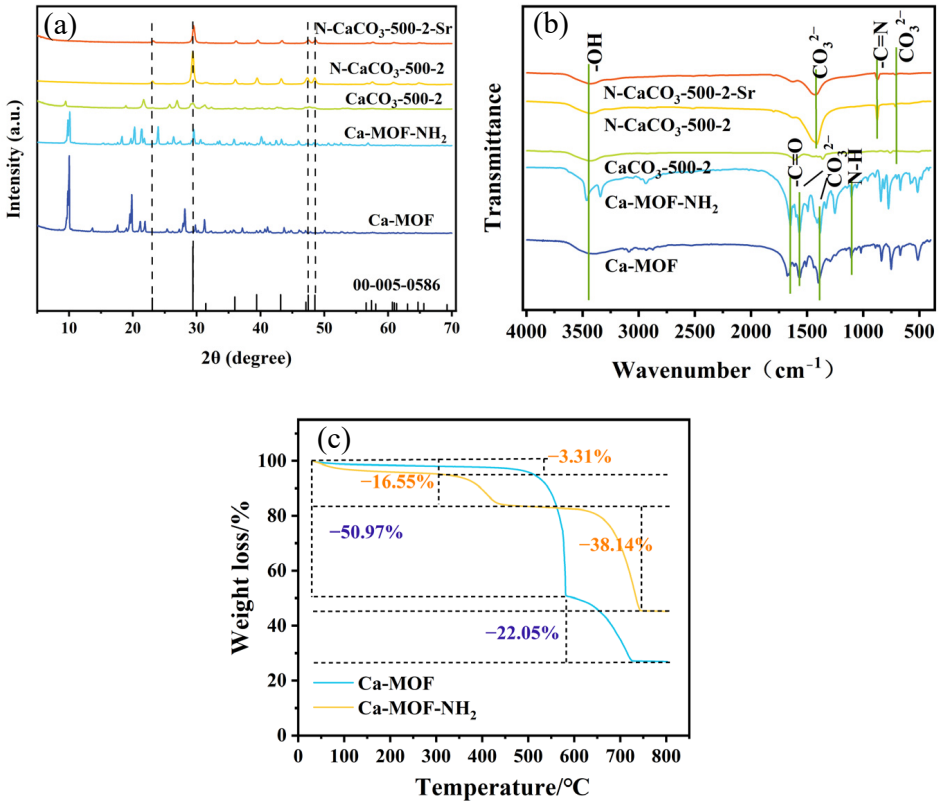

Figure 2. (**a**) XRD patterns and (**b**) FTIR spectra of Ca-MOFs, $CaCO_3$-500-2, N-$CaCO_3$-500-2, N-$CaCO_3$-500-2-Sr; (**c**) TG curves of Ca-MOFs.

As shown by the FTIR spectra of the Ca-MOFs and its derivatives (Figure 2b), the observed absorption peaks at 732 cm^{-1} and 1564~1384 cm^{-1} represent the in-plane bending vibration, out-of-plane bending vibration, and asymmetric stretch vibration of the carbonate ions, respectively [41]. The bending vibrations of amino N-H corresponded to the peaks at 1107 cm^{-1} and the absorption band at 810 cm^{-1} belonged to -C=N- [41]. The adsorption peak at 1632 cm^{-1} represented the characteristic adsorption of -COOH on C=O bonds in H_2BDC and the absorption peak at 3435 cm^{-1} represented the stretching vibration of -OH on the benzene ring [42,43].

TG is used to investigate the thermal stability and quantify the components of Ca-MOFs. Figure 2c clearly shows that below 200 °C, 3.31% of the weight loss could be attributed to the evaporation of adsorbed water molecules [44]. The weight loss at 300–550 °C indicated the presence of oxygen-containing groups on the surface of the Ca-MOFs that were converted into CO_2, as well as the high-temperature decomposition of -NH_2. At about 600 °C, a dramatic weight loss was observed, implying the destruction of the framework of the Ca-MOFs and the decomposition of its organic linkers [45].

As shown in Figure 3a, the pore size and specific surface area of the Ca-MOFs were relatively small. In Figure 3b, the N_2 adsorption–desorption curve of N-$CaCO_3$-500-2 exhibited a type IV structure, with pore sizes mainly concentrated in the range of 2–20 nm. As a result of the analysis of the data presented in Table 1, we found that the specific surface area of N-$CaCO_3$-500-2 (136.53 m^2/g) was much larger than that of Ca-MOF-NH_2 (0.39 m^2/g), indicating that high-temperature calcination can create a significant abundance of pores. Additionally, the specific surface area of $CaCO_3$-500-2 and N-$CaCO_3$-500-2 were calculated to be 62.39 m^2/g and 136.53 m^2/g, respectively. This suggested that N-doping endowed the structure of $CaCO_3$ with rich coordination defects and a big pore size, probably conducive to pollutant diffusion and adsorption. This unique structure can provide more active sites for Sr(II) adsorption. The average pore size of N-$CaCO_3$-500-2 was 10.58 nm and the pore volume was 0.44 cm^3/g, and these structural features may be responsible for the excellent adsorption performance of N-$CaCO_3$-500-2.

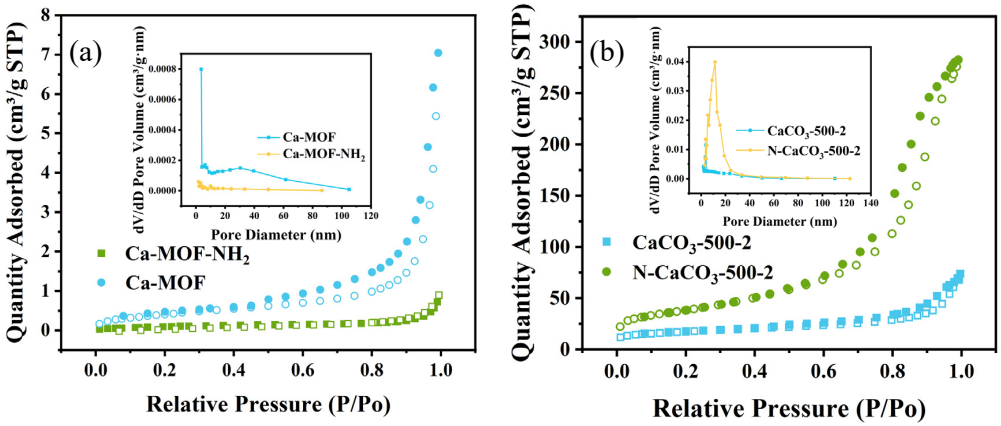

Figure 3. N_2 adsorption–desorption isotherms of (**a**) Ca-MOF and Ca-MOF-NH_2, (**b**) $CaCO_3$-500-2 and N-$CaCO_3$-500-2.

Table 1. Surface area, average pore diameter, and pore volume of parent Ca-MOF, Ca-MOF-NH_2, and calcined $CaCO_3$-500-2, N-$CaCO_3$-500-2.

Sample	Ca-MOF	Ca-MOF-NH_2	$CaCO_3$-500-2	N-$CaCO_3$-500-2
BET surface area (m^2/g)	1.55	0.39	62.39	136.53
Average pore diameter (nm)	20.84	16.19	10.33	10.58
Pore volume (cm^3/g)	0.011	0.0014	0.11	0.44

The effect of N-doping on the structures was analyzed by using XPS spectroscopy. As shown in Figure 4a, in regard to the full spectrum for $CaCO_3$-500-2 and N-$CaCO_3$-500-2, C1s, Ca2p, and O1s peaks were observed. Additionally, the full spectrum for N-$CaCO_3$-500-2 revealed an extra peak at N1s, indicating successful N-doping of $CaCO_3$. Figure 4b shows that N existed as metal nitrides and C-N in the materials. Figure 4c,d reveals that the intensity of the Ca2p peak appeared to be reduced due to nitrogen doping of $CaCO_3$, suggesting an interaction between Ca and N atoms. Additionally, the peak slightly shifted toward the higher binding energy direction, indicating that nitrogen doping had become integrated into the lattice of $CaCO_3$. This incorporation altered the electron cloud distribution of the surrounding atoms and facilitated the formation of new chemical bonds, resulting in changes to the binding energy of the atoms near the doping site. This suggests that N-doping adjusted the electronic structure of $CaCO_3$, which may show some unique properties in regard to surface adsorption [46–48].

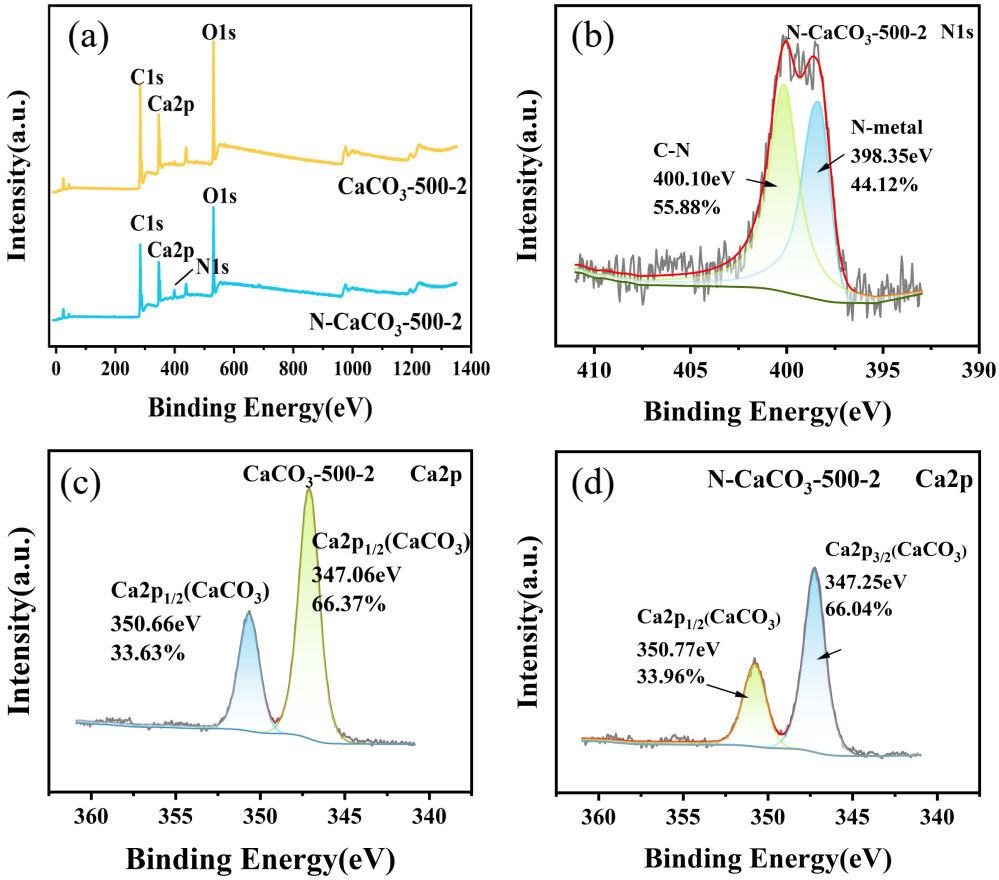

Figure 4. High-resolution XPS spectra: (**a**) full spectrum diagram of $CaCO_3$-500-2 and N-$CaCO_3$-500-2, (**b**) N1s in N-$CaCO_3$-500-2, (**c**) Ca2p in $CaCO_3$-500-2, (**d**) Ca2p in N-$CaCO_3$-500-2.

3.2. Evaluation of Sr(II) Adsorption Performance

3.2.1. Effect of Different Materials

Ca-MOF, Ca-MOF-NH_2, their calcination products, and commercial $CaCO_3$, were applied for Sr(II) adsorption to evaluate their adsorption performance. These materials were allowed to adsorb Sr(II) in certain conditions. In Figure 5a, the removal efficiency of N-$CaCO_3$-500-2 (38.54%) was greater than that of commercial $CaCO_3$ (1.24%), Ca-MOFs, and $CaCO_3$-500-2. The removal efficiency of N-$CaCO_3$-500-2 was approximately 30 times that of commercial $CaCO_3$. The results show that N-doping can change the compact microstructure of $CaCO_3$, improve its mass transfer capacity, and enhance its adsorption

performance. Regarding the calcination time of N-$CaCO_3$ (Figure 5b), this material, with a calcination time of 2 h, exhibited the highest adsorption efficiency for Sr(II) removal. A longer calcination time may damage the porous structure and decompose the functional groups of the materials. Concerning the calcination temperature of N-$CaCO_3$-2 (Figure 5c), N-$CaCO_3$-500-2 had the highest adsorption efficiency for Sr(II) removal. As a result of calcination, N-$CaCO_3$-500-2 developed a unique porous structure and possessed internal active sites that were available for Sr(II) adsorption. Therefore, N-$CaCO_3$-500-2 was used to conduct the subsequent adsorption experiments.

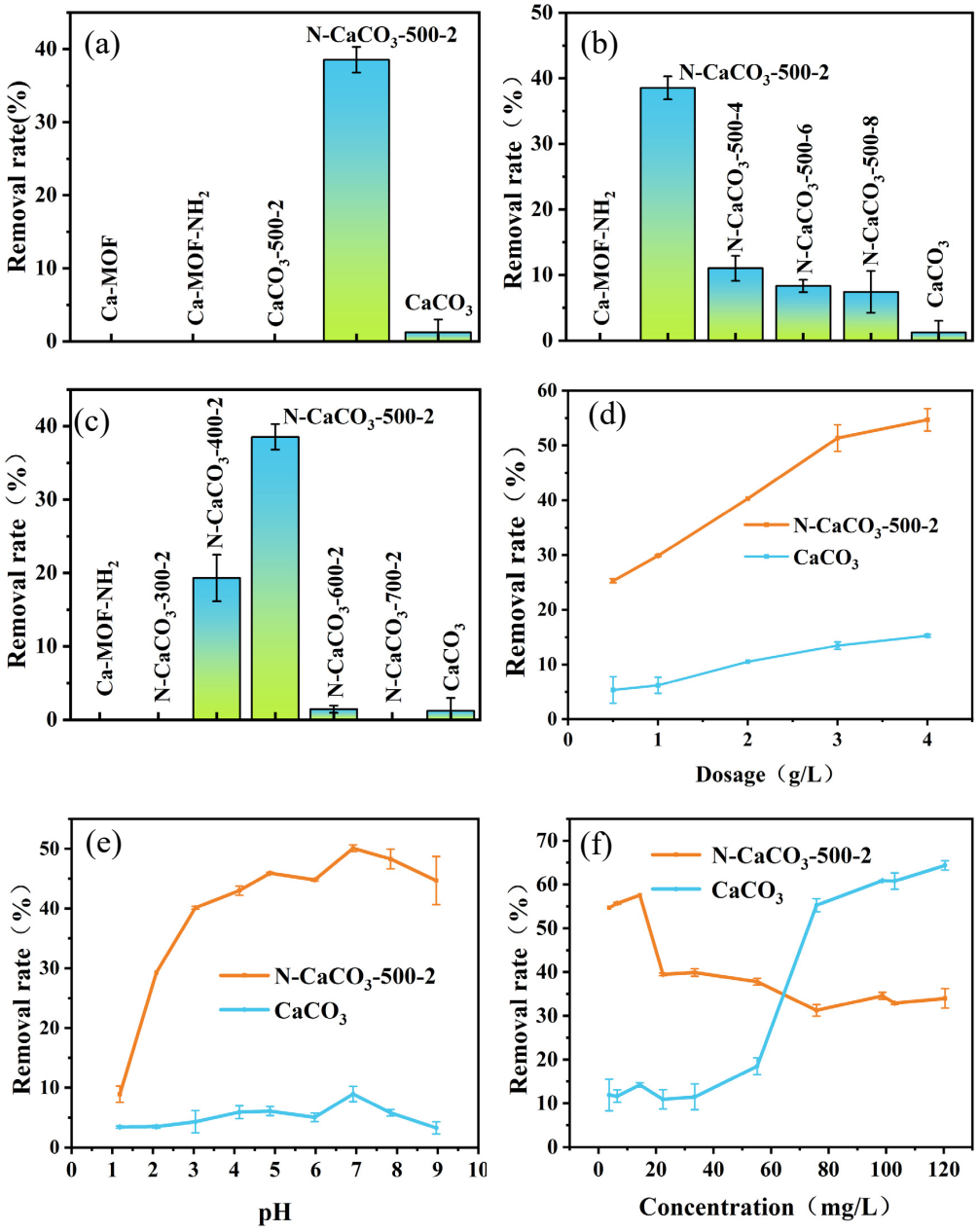

Figure 5. (**a**) Effect of different materials on Sr(II) adsorption by Ca-MOFs (C_0 = 4.45 mg·L^{-1}, m_{ads}/V_{sol} = 2 g·L^{-1}, pH = 6.24, t = 24 h), (**b**) Sr(II) adsorption performance by Ca-MOFs with different calcination times (C_0 = 4.45 mg·L^{-1}, m_{ads}/V_{sol} = 2 g·L^{-1}, pH = 6.24; t = 24 h), (**c**) Sr(II) adsorption performance of Ca-MOFs at different temperatures (C_0 = 4.45 mg·L^{-1}, m_{ads}/V_{sol} = 2 g·L^{-1}, pH = 6.24; t = 24 h), (**d**) effect of dosage on Sr(II) adsorption by N-$CaCO_3$-500-2 and $CaCO_3$ (C_0 = 5.24 m·L^{-1}, t = 24 h, pH = 6.24), (**e**) effect of pH on Sr(II) adsorption by N-$CaCO_3$-500-2 and $CaCO_3$ (C_0 = 5 mg·L^{-1}, t = 24 h, m_{ads}/V_{sol} = 3 g·L^{-1}), (**f**) effect of initial concentration of Sr(II) on its adsorption by N-$CaCO_3$-500-2 and $CaCO_3$ (pH = 7, t = 24 h, m_{ads}/V_{sol} = 3 g·L^{-1}).

3.2.2. Effect of Adsorbent Dosage

As shown in Figure 5d, the adsorption efficiency of N-$CaCO_3$-500-2 was generally 4.5 times higher than that of commercial $CaCO_3$. When the dosage increased from 0.5 g/L to 3 g/L, the removal efficiency in regard to Sr(II) doubled from 25.29% to 51.24%. However, with a further increase to 4 g/L, the removal efficiency only grew to 54.68%, showing a slower rate. As the dosage increased, more adsorption sites were available for Sr(II), leading to an increase in removal efficiency. When the adsorbent dosage continued to increase, an adverse effect on adsorption may appear, to some extent, probably due to the agglomeration of the adsorbent. Therefore, the adsorbent dosage was set at 3 g/L in the following experiments [49].

3.2.3. Effect of the Initial pH

The solution pH, as a key factor, usually has a strong influence on the interfacial adsorption process. Figure 5e indicates that the pH range of the Sr(II) solution was 1~9, and the removal efficiency in terms of Sr(II) by N-$CaCO_3$-500-2 was markedly higher than that of commercial $CaCO_3$. When the pH = 5–7, the removal efficiency of N-$CaCO_3$-500-2 was above 45%. The removal efficiency of N-$CaCO_3$-500-2 was the highest (50.10%) at pH 7 and, at this time, the removal efficiency of commercial $CaCO_3$ in regard to Sr(II) was 8.96%. In an acidic environment, Sr(II) was relatively stable. The high concentration of H^+ competed with Sr(II), making it less prone to complexation reactions. In this case, adsorption was predominantly influenced by electrostatic attraction. An acidic pH was obviously able to change the pore structure of the adsorbent, thus affecting the adsorption efficiency in regard to Sr(II). In neutral conditions, the concentration of OH^- was relatively low, leading to a weak complexing effect with Sr(II). Consequently, the amount of $Sr(OH)_2$ produced was trivial and exerted a negligible impact on the adsorption process. At a high pH, the concentration of OH^- rose significantly, enhancing the complexing effect between Sr(II) and OH^- and resulting in the formation of various strontium hydroxide complexes. The formation of these complexes altered the existing form and activity of strontium in the solution, thereby influencing the adsorption efficacy. Therefore, the following experiments were fixed at pH = 7 to ensure the best performance of N-$CaCO_3$-500-2 [50].

3.2.4. Effect of the Initial Concentration

The adsorption amount at different initial concentrations of Sr(II) is shown in Figure 5f. It was observed that the adsorption by N-$CaCO_3$-500-2 at low Sr(II) concentrations was better than that at high concentrations. The removal efficiency increased at low concentrations, peaked (57.57%) at 15 mg/L, and decreased at 20 mg/L and beyond. In contrast, the maximum adsorption capacity of commercial $CaCO_3$ increased from 11.68% to 64.39% when the initial Sr(II) concentration increased from 5 to 120 mg/L. Thus, N-$CaCO_3$-500-2 exhibited the highest removal efficiency at a Sr(II) concentration below 64.5 mg/L, whereas modest adsorption happened at a concentration greater than 64.5 mg/L. It is suggested that there may be sufficient adsorption sites on the adsorbent surface to adsorb Sr(II) at a low Sr(II) concentration. At high Sr(II) concentrations, the strontium ions may mainly exist as $Sr(OH)^+$ due to hydrolysis reactions, and this situation would weaken the adsorption interaction between Sr(II) and the active sites, which negatively impacts the adsorption efficiency of the as-prepared N-$CaCO_3$-500-2. A Sr(II) concentration of 5 mg/L was chosen to complete the subsequent adsorption experiments [51].

3.2.5. Adsorption Kinetics

The kinetic data on N-$CaCO_3$-500-2 and commercial $CaCO_3$ adsorbing Sr(II) within 20 h were studied using the pseudo-first-order model (PFO) [52] and pseudo-second-order model (PSO), as shown in Figure 6a. The kinetic parameters are shown in Table 2. It can be seen that they showed similar trends, rapidly adsorbing Sr(II) in the first 120 min, followed by a slow increase in adsorption efficiency, until reaching adsorption equilibrium. The kinetic model formulas are given as follows [53]:

$$\text{PFO}: \ q_t = q_e\left(1 - e^{-k_1 t}\right) \tag{2}$$

$$\text{PSO}: \ q_t = \frac{q_e^2 k_2 t}{q_e k_2 t + 1} \tag{3}$$

where t is the contact time (min), q_e and q_t (mg·g^{-1}) are the amount of Sr(II) adsorbed at the adsorption equilibrium and at time t, respectively, and k_1 (min^{-1}) is the pseudo primary rate constant, and k_2 (g·mg^{-1}·min^{-1}) is the pseudo secondary rate constant. As shown in Table 2, the correlation coefficient of the first-order kinetics was 0.9516 and the second-order kinetics was 0.9964, indicating that the pseudo-second-order kinetic model was more appropriate to describe the Sr(II) adsorption process. The calculated removal efficiency of N-$CaCO_3$-500-2 (45.65%) was close to the experimental value of 44.88%, indicating that the adsorption process was mainly controlled by chemical adsorption.

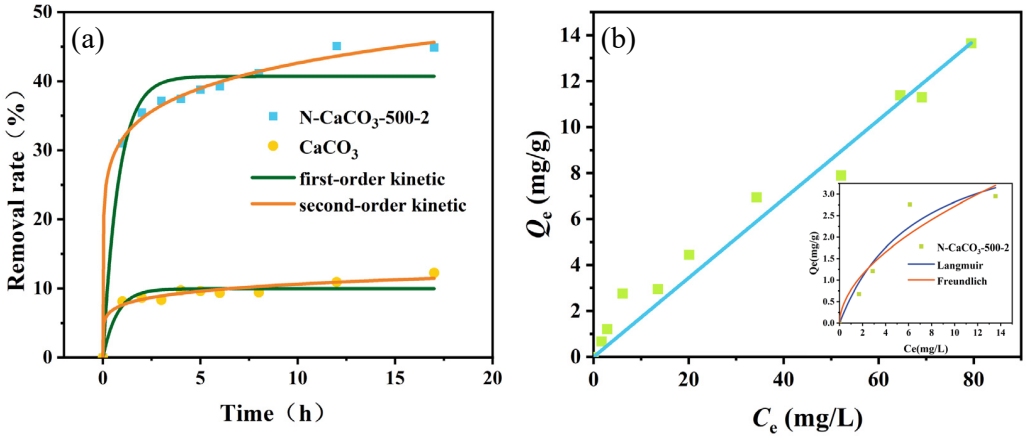

Figure 6. (**a**) Kinetic study of Sr(II) adsorption process (C_0 = 4.98 mg·L^{-1}, pH = 7.42, m_{ads}/V_{sol} = 3 g·L^{-1}) and (**b**) isothermal studies of Sr(II) adsorption process (pH = 7, t = 24 h, m_{ads}/V_{sol} = 3 g·L^{-1}).

Table 2. Kinetic model parameters for the adsorption of Sr(II).

Adsorbents	Pseudo-First-Order Model R_1^2	Pseudo-Second-Order Model R_2^2
N-$CaCO_3$-500-2	0.9516	0.9964
$CaCO_3$	0.8825	0.9714

3.2.6. Adsorption Isotherms

To further understand the adsorption behavior between adsorbates and adsorbents, adsorption isotherm experiments were conducted at 25 °C for different initial concentrations of Sr(II) (3–120 mg·L^{-1}) and the Langmuir model and the Freundlich model were

applied to analyze the intrinsic process of the adsorption. The corresponding formulas are given as follows [54]:

$$\text{Langmuir}: \ q_e = \frac{k_L q_m C_e}{1 + k_L C_e} \quad (4)$$

$$\text{Freundlich}: \ q_e = k_F C_e^{1/n} \quad (5)$$

where q_e (mg·g^{-1}) and C_e (mg·L^{-1}) represent the adsorption capacity and Sr(II) concentration at the adsorption equilibrium, respectively, q_m (mg·L^{-1}) represents the maximum adsorption capacity, k_L represents the Langmuir constant, and n and k_F represent the Freundlich constants. In Figure 6b, with the increase in the initial Sr(II) concentration, the removal efficiency of N-$CaCO_3$-500-2 gradually increased, implying that the ion exchange model was more appropriate to describe the adsorption process. It is worth noting that when the concentration of Sr(II) was low, the adsorption was fitted by the Langmuir at $R^2 \approx 0.83$ and the Freundlich model at $R^2 \approx 0.86$ [50], indicating that the adsorption process involved multi-layer adsorption. The fitting results imply that the adsorption may not completely comply with the assumption concerning homogeneous surface adsorption and there may have been a certain degree of heterogeneity underlying the adsorption interactions. This may explain the complicatedness of the adsorption mechanism, where different adsorption mechanisms may happen simultaneously between an adsorbent and an adsorbate and may be influenced by various factors. At high concentrations of Sr(II), the graph follows a straight path, which aligns with the ion exchange model.

As illustrated in Table 3, the adsorption capacity of N-$CaCO_3$-500-2 for Sr(II) removal was comparable to other materials. Notably, under the specified conditions in terms of the dosage, equilibrium time, reaction temperature, and initial Sr(II) concentration, N-$CaCO_3$-500-2 demonstrated superior adsorption capacity for Sr(II) compared to the low-cost clay adsorbent, montmorillonite. This indicates that N-$CaCO_3$-500-2 offers several advantages.

Table 3. Comparison of different adsorbents in regard to their adsorption characteristics.

Adsorbents	Q_e (mg/g)	t_e (h)	m/V (g/L)	C_0 (mg/L)	T (°C)	Reference
Clinoptilolite	6.7	120	50	300	60	[55]
GMZ bentonite	9.72	1	10	100	25	[56]
Ca-type BentonilWRK Montmorillonite	0.35	24	5	4.4	25	[57]
N-$CaCO_3$-500-2	0.76	24	3	5	25	This work

3.3. Adsorption Mechanisms

According to the BET results, N-$CaCO_3$-500-2 had a larger specific surface area, which meant that there were more collisions between Sr(II) and N-$CaCO_3$-500-2, thus promoting the occurrence of adsorption.

It is envisaged that the substitutional effect of Sr(II) on MOF structures was responsible for the removal of Sr(II) from the aqueous solution. Such a mechanism was confirmed by the morphological changes in the composites, as shown in Figure 7. Before adsorption, N-$CaCO_3$-500-2 exhibited a porous structure, with an ordered and compact arrangement (Figure 7a). However, while the porous structure maintained its regular and neat arrangement after adsorption, the surface of the adsorbent appeared to be smoother than before adsorption (Figure 7b). This proves that Sr(II) was successfully attached to the adsorbent surface.

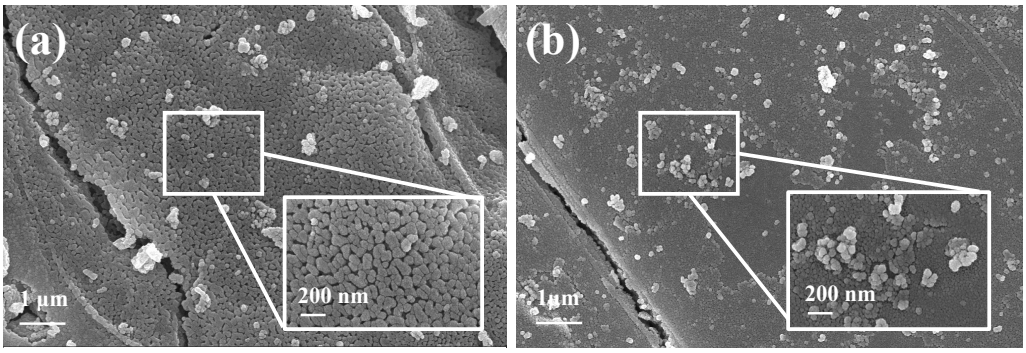

Figure 7. SEM images of (**a**) N-$CaCO_3$-500-2, (**b**) N-$CaCO_3$-500-2-Sr.

Based on the data presented in Figure 8, it is evident that the energy spectrum of the material displayed an increase in the Sr(II) peak after adsorption, whereas the peaks of Ca and N were weakened. The content of Sr(II) increased from 0.06% to 2.99% after the reaction. On the other hand, the content of the nitrogen atoms disappeared and that of Ca(II) decreased to 35.56% from 51.88%. This supported the conclusion that Sr(II) was effectively adsorbed, with calcium ions and N-containing groups acting as active sites.

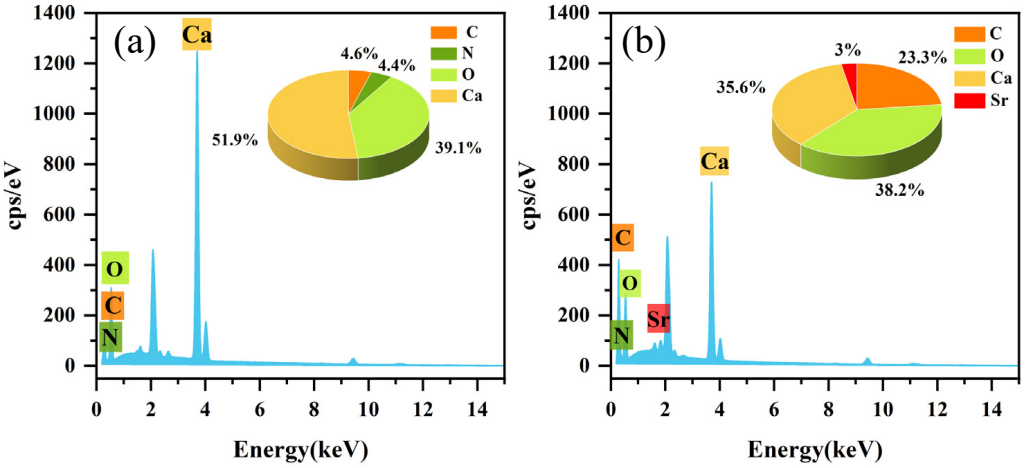

Figure 8. EDS images of (**a**) N-$CaCO_3$-500-2, (**b**) N-$CaCO_3$-500-2-Sr.

It is evident that the removal efficiency increased with the increase in pH. This observation suggests that N-$CaCO_3$-500-2 is combined with OH^- in water, resulting in the formation of surface hydroxyls (sorbent-OH). Subsequently, these active hydroxyls interacted with Sr(II) to form surface complexation.

The XPS spectra of N-$CaCO_3$-500-2 were used to study the interaction sites of N-$CaCO_3$-500-2 and Sr(II) (Figure 9). To investigate the adsorption process of N-$CaCO_3$-500-2 in regard to Sr(II), the spectra of C1s, O1s, N1s, and Ca2p of N-$CaCO_3$-500-2 before and after adsorption were analyzed. The appearance of Sr3d in N-$CaCO_3$-500-2-Sr after adsorption demonstrated the adsorption of Sr(II) by the adsorbent (Figure 9a). Figure 9b shows the Sr3d peak at 133.73 eV, indicating the formation of $SrCO_3$ due to the Sr(II) ion exchange with $CaCO_3$ during adsorption.

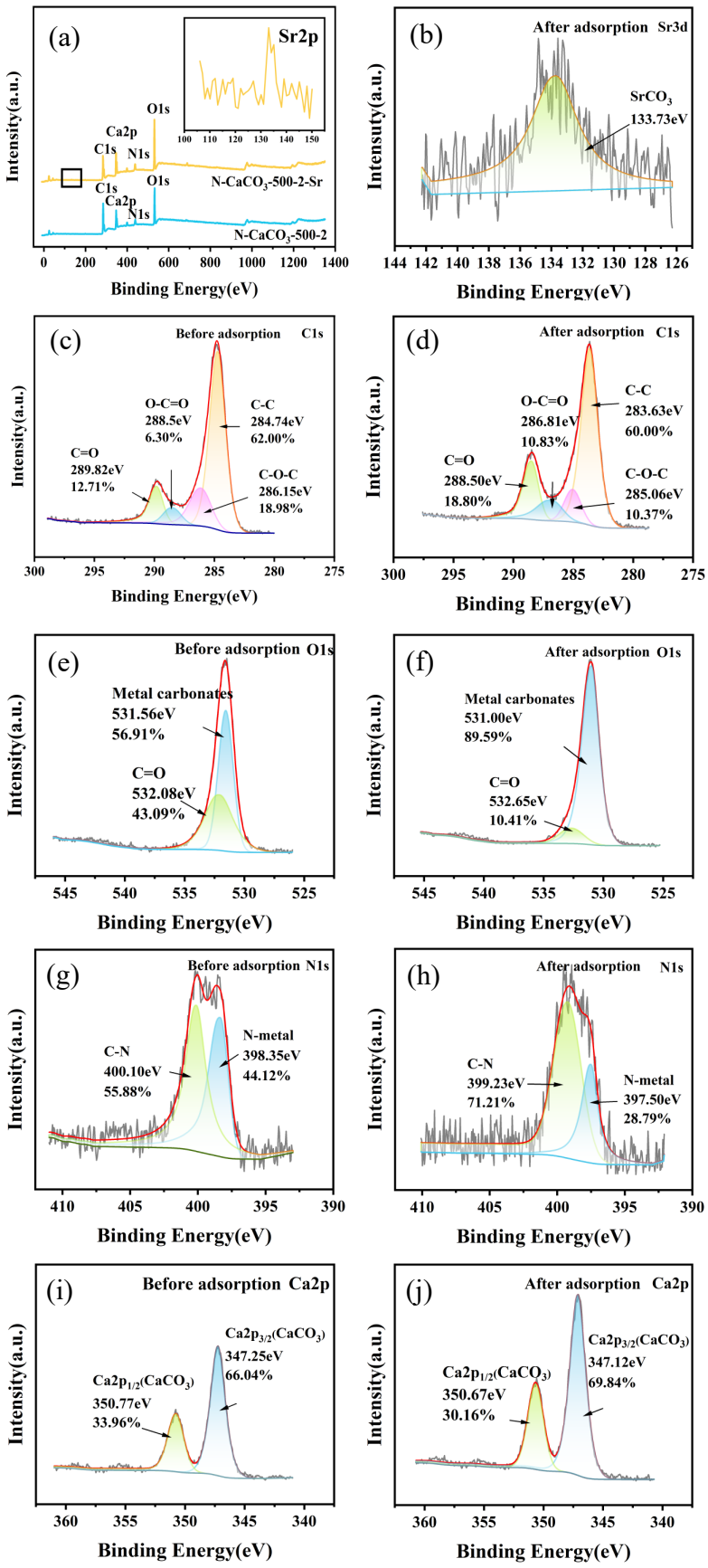

Figure 9. High-resolution XPS spectra of full spectrum diagram: (**a**) C1s (**c**,**d**), O1s (**e**,**f**), N1s (**g**,**h**), and Ca2p (**i**,**j**) of N-$CaCO_3$-500-2 before and after Sr(II) adsorption, and Sr3d (**b**) of N-$CaCO_3$-500-2 after Sr(II) adsorption.

Figure 9c,d show the C1s spectra in the C=O, O-C=O, C-C, and C-O-C bonds, respectively. The relative amount of the O-C=O, C=O bond increased by 4.53% and 7.97%, while the relative amount of C-C and C-O-C bonds decreased by 2% and 8.61%, respectively.

As illustrated in Figure 9e,f, the O1s spectrum of N-$CaCO_3$-500-2 was characterized by two distinct peaks, which correspond to the C=O bond and metal carbonate bonds, respectively. Notably, the relative intensity of the C=O bond decreased by 32.68%, while the relative intensity of the metal carbonate bonds increased by the same percentage. This observation can be attributed to the interaction between Sr(II) and CO_3^{2-} in regard to N-$CaCO_3$-500-2.

As shown in Figure 9g,h, the N1s spectrum of N-$CaCO_3$-500-2 was divided into two peaks, corresponding to the C-N and N-metal bond, respectively. The relative amount of the N-metal bond decreased by 15.33%, while the relative amount of C-N bonds increased by 15.33%. The above results prove that the nitrogen-containing groups played an important role in the adsorption process.

In Figure 9i,j, the Ca2p spectrum of N-$CaCO_3$-500-2 was divided into two peaks, corresponding to the $Ca2p_{1/2}$ and $Ca2p_{3/2}$ bond, respectively. The relative amount of the $Ca2p_{1/2}$ bond decreased by 3.8%, while the relative amount of $Ca2p_{3/2}$ bonds increased by 3.8%. After adsorption, the peaks of $CaCO_3$ shifted towards the lower binding energy location. This phenomenon indicates that during the adsorption process, Sr(II) strongly interacted with $CaCO_3$, leading to a decrease in the electron cloud density around the Ca. This could be explained as a result of the ion exchange between Sr(II) and Ca(II) [28].

According to the above analysis, the adsorption mechanism of N-$CaCO_3$-500-2 was inferred and depicted as follows (Figure 10). One possible mechanism is that Sr^{2+} replaced Ca^{2+} to produce $SrCO_3$. The reaction equation could be described as $CaCO_3 + Sr^{2+} \rightarrow SrCO_3 + Ca^{2+}$. The other is that surface OH^- interacted with Sr^{2+} to form surface complexation (sorbent-O-Sr). Obviously, the former was dominant in regard to this adsorption process. These facts suggest that N-doped $CaCO_3$ changed the compact structure and provided enough space for pollutant transfer and facilitated the adsorption process.

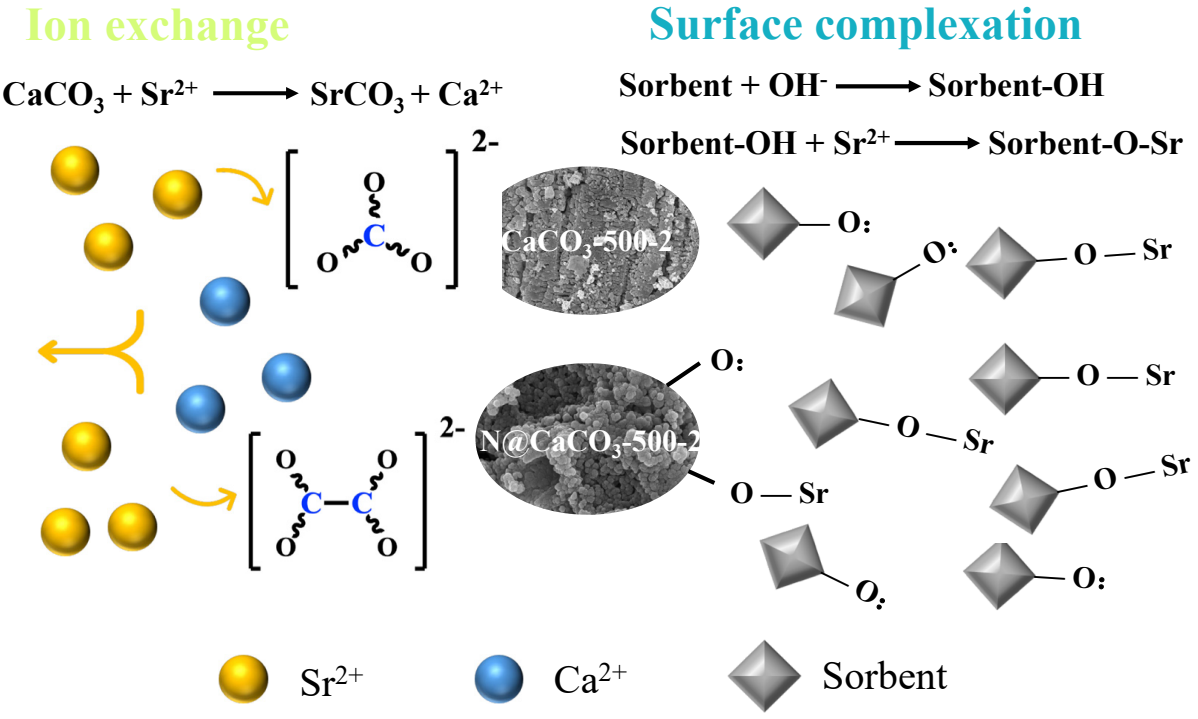

Figure 10. Schematic presentation of Sr(II) adsorption mechanism involving N-$CaCO_3$-500-2.

4. Conclusions

In this study, N-$CaCO_3$ was first synthesized using a method combining solvothermal treatment and calcination, which showed good adsorption performance for Sr(II). The structural characterizations indicated that the successful doping of N in calcite resulted in a more ordered structure, a higher specific surface area, and the increased formation of mesopores. The results of the batch adsorption experiments showed that the pseudo-second-order kinetic model (R^2 = 0.9964) and the ion exchange model (R^2 = 0.9859) fitted the adsorption well, confirming the nature of the chemisorption. N-$CaCO_3$ exhibited a removal rate of over 40% for Sr(II), within a wide pH range from 3.0 to 9.0, and the optimal pH value was 7.0. The as-synthesized N-$CaCO_3$ showed good adsorption performance in regard to low concentrations of Sr(II). The adsorption mechanism mainly involved ion exchange and surface complexation, with the former dominating the adsorption process, indicating that Ca and N played important roles in the adsorption process. N-doped calcite can effectively adsorb Sr(II) in nuclear wastewater, which is meaningful for radionuclide cleanup and is worthy of more in-depth study.

Author Contributions: X.X.: investigation, formal analysis, writing–original draft. J.H. and Q.D.: conceptualization, writing—review and editing, supervision. X.Z.: supervision. G.Y.: supervision, funding, writing—review and editing. All authors have read and agreed to the published version of the manuscript.

Funding: This work was supported by a research program by the State Administration of Science, Technology and Industry for National Defence, China ([2017]1474), and was partly funded by the Research Fund of Tianjin Key Laboratory of Aquatic Science and Technology and Xiamen Key Laboratory of Municipal and Industrial Solid Waste Utilization and Pollution Control (KHX2022-059).

Institutional Review Board Statement: Not applicable.

Informed Consent Statement: Not applicable.

Data Availability Statement: The raw data supporting the conclusions in this article will be made available by the authors upon request.

Conflicts of Interest: The authors declare that they have no known competing financial interests or personal relationships that could have appeared to influence the work reported in this paper.

References

1. Cheng, J.; Liu, K.; Li, X.; Huang, L.; Liang, J.; Zheng, G.; Shan, G. Nickel-metal-organic framework nanobelt based composite membranes for efficient Sr^{2+} removal from aqueous solution. *Environ. Sci. Ecotechnol.* **2020**, *3*, 100035. [CrossRef] [PubMed]
2. Yin, L.; Kong, X.; Shao, X.; Ji, Y. Synthesis of DtBuCH18C6-coated magnetic metal–organic framework Fe_3O_4@ UiO-66-NH_2 for strontium adsorption. *J. Environ. Chem. Eng.* **2019**, *7*, 103073. [CrossRef]
3. Zhang, J.; Chen, L.; Dai, X.; Zhu, L.; Xiao, C.; Xu, L.; Zhang, Z.; Alekseev, E.V.; Wang, Y.; Zhang, C. Distinctive two-step intercalation of Sr2+ into a coordination polymer with record high 90Sr uptake capabilities. *Chem* **2019**, *5*, 977–994. [CrossRef]
4. Choi, J.-W.; Park, Y.-J.; Choi, S.-J. Synthesis of metal–organic framework ZnO x-MOF@ MnO_2 composites for selective removal of strontium ions from aqueous solutions. *ACS Omega* **2020**, *5*, 8721–8729. [CrossRef]
5. Abass, M.R.; Eid, M.A.; Ibrahim, A.B. Silico antimonate nanocomposite material: I-preparation, characterization and its application for separation of strontium and rubidium from aqueous solutions. *Int. J. Environ. Anal. Chem.* **2024**, *104*, 2776–2791. [CrossRef]
6. Park, B.; Ghoreishian, S.M.; Kim, Y.; Park, B.J.; Kang, S.-M.; Huh, Y.S. Dual-functional micro-adsorbents: Application for simultaneous adsorption of cesium and strontium. *Chemosphere* **2021**, *263*, 128266. [CrossRef]
7. Liu, R.; Chen, G.; Wang, Z.; Zhao, Q.; Wu, L.; Li, Q.; Tian, R.; Chen, X.; Li, X.; Chen, Z. Calcium-intercalated zirconium phosphate by granulation: A strategy for enhancing adsorption selectivity of strontium and cesium from liquid radioactive waste. *Inorg. Chem.* **2023**, *62*, 5799–5809. [CrossRef] [PubMed]
8. Rashad, G.M.; Mahmoud, M.R.; Soliman, M.A. Combination of coprecipitation and foam separation processes for rapid recovery and preconcentration of cesium radionuclides from water systems. *Process Saf. Environ. Prot.* **2019**, *130*, 163–173. [CrossRef]

9. Yang, L.; Hu, W.; Chang, Z.; Liu, T.; Fang, D.; Shao, P.; Shi, H.; Luo, X. Electrochemical recovery and high value-added reutilization of heavy metal ions from wastewater: Recent advances and future trends. *Environ. Int.* **2021**, *152*, 106512. [CrossRef] [PubMed]
10. Campbell, E.L.; Westesen, A.M.; Williams, A.N.; Peterson, R.A. Effect of Na concentration on Cs distribution with crystalline silicotitanate in tank waste simulants. *Ind. Eng. Chem. Res.* **2023**, *62*, 7650–7656. [CrossRef]
11. Xu, X.; Lv, H.; Zhang, M.; Wang, M.; Zhou, Y.; Liu, Y.; Yu, D.-G. Recent progress in electrospun nanofibers and their applications in heavy metal wastewater treatment. *Front. Chem. Sci. Eng.* **2023**, *17*, 249–275. [CrossRef]
12. Zhao, D.; Cheah, W.Y.; Lai, S.H.; Ng, E.-p.; Khoo, K.S.; Show, P.L.; Ling, T.C. Symbiosis of microalgae and bacteria consortium for heavy metal remediation in wastewater. *J. Environ. Chem. Eng.* **2023**, *11*, 109943. [CrossRef]
13. Hong, H.-J.; Ryu, J.; Park, I.S.; Ryu, T.; Chung, K.S.; Kim, B.G. Investigation of the strontium (Sr(II)) adsorption of an alginate microsphere as a low-cost adsorbent for removal and recovery from seawater. *J. Environ. Manag.* **2016**, *165*, 263–270. [CrossRef]
14. Paz, R.; Viltres, H.; Gupta, N.K.; Leyva, C.; Dhavale, R.P.; Park, H.H.; Romero-Galarza, A.; Rajabzadeh, A.R.; Srinivasan, S. High-capacity adsorptive removal and recovery of trivalent europium ions using zinc-based metal–organic frameworks: Adsorption and mechanism study. *Inorg. Chem. Commun.* **2023**, *155*, 111049. [CrossRef]
15. Elewa, K.; Belal, A.; El Monayeri, O.; Tawfic, A. Application of metal-organic framework (Zn-Ph-D CP) for copper ion removal from aqueous solution. *Ain Shams Eng. J.* **2022**, *13*, 101670. [CrossRef]
16. Qu, G.; Jia, P.; Zhang, T.; Li, Z.; Chen, C.; Zhao, Y. UiO-66 (Zr)-derived t-zirconia with abundant lattice defect for remarkably enhanced arsenic removal. *Chemosphere* **2022**, *288*, 132594. [CrossRef] [PubMed]
17. Gupta, K.; Yuan, B.; Chen, C.; Varnakavi, N.; Fu, M.-L. K2xMnxSn3− xS6 (x= 0.5–0.95)(KMS-1) immobilized on the reduced graphene oxide as KMS-1/r-GO aerogel to effectively remove Cs+ and Sr2+ from aqueous solution. *Chem. Eng. J.* **2019**, *369*, 803–812. [CrossRef]
18. Zhang, T.; Wang, W.; Zhao, Y.; Bai, H.; Wen, T.; Kang, S.; Song, G.; Song, S.; Komarneni, S. Removal of heavy metals and dyes by clay-based adsorbents: From natural clays to 1D and 2D nano-composites. *Chem. Eng. J.* **2021**, *420*, 127574. [CrossRef]
19. Han, H.; Rafiq, M.K.; Zhou, T.; Xu, R.; Mašek, O.; Li, X. A critical review of clay-based composites with enhanced adsorption performance for metal and organic pollutants. *J. Hazard. Mater.* **2019**, *369*, 780–796. [CrossRef]
20. Zhang, Y.; Wang, B.; Cheng, Q.; Li, X.; Li, Z. Removal of toxic heavy metal ions (Pb, Cr, Cu, Ni, Zn, Co, Hg, and Cd) from waste batteries or lithium cells using nanosized metal oxides: A review. *J. Nanosci. Nanotechnol.* **2020**, *20*, 7231–7254. [CrossRef] [PubMed]
21. Kim, M.; Yoon, Y.; Kim, J.; Choi, S.; Choi, S.; Lee, S. Evaluation of the adsorption potential of iron and manganese oxide immobilized sand for the removal of Cs (I) and Sr (II) from aquatic environment. *Desalination Water Treat.* **2018**, *135*, 268–278.
22. Jiang, Y.; Liu, C.; Huang, A. EDTA-functionalized covalent organic framework for the removal of heavy-metal ions. *ACS Appl. Mater. Interfaces* **2019**, *11*, 32186–32191. [CrossRef]
23. Liu, P.; Yang, P.; Yang, J.; Gu, J. One-pot synthesis of sulfonic acid functionalized Zr-MOFs for rapid and specific removal of radioactive Ba^{2+}. *Chem. Commun.* **2021**, *57*, 5822–5825. [CrossRef] [PubMed]
24. Fu, X.; Liu, J.; Ren, Z.; Zhang, S.; Xiao, F.; Peng, G. Introduction of phosphate groups into metal-organic frameworks to synthesize MIL-101 (Cr)-PMIDA for selective adsorption of U (VI). *J. Radioanal. Nucl. Chem.* **2022**, *331*, 889–902. [CrossRef]
25. Chen, X.; Ma, H.; Ji, X.; Han, R.; Pang, K.; Yang, Z.; Liu, Z.; Peng, S. Engineering green MOF-based superhydrophobic sponge for efficiently synchronous removal of microplastics and pesticides from high-salinity water. *Water Res.* **2023**, *243*, 120314. [CrossRef] [PubMed]
26. Liang, P.-C.; Liu, H.-K.; Yeh, C.-T.; Lin, C.-H.; Zima, V. Supramolecular assembly of calcium metal−organic frameworks with structural transformations. *Cryst. Growth Des.* **2011**, *11*, 699–708. [CrossRef]
27. Xu, X.; Feng, F.; Wan, Z.; Wang, Y.; Yu, M.; Han, X.; Wu, G.; Xing, W. Rapid electron transfer reinforced by interfacial Co-O bonding in MOF/COF hybrids for highly efficient degrade tetracycline by activating peroxymonosulfate. *Colloids Surf. A Physicochem. Eng. Asp.* **2024**, *689*, 133686. [CrossRef]
28. Ma, Y.; You, D.; Fang, Y.; Luo, J.; Pan, Q.; Liu, Y.; Wang, F.; Yang, W. Confined growth of MOF in chitosan matrix for removal of trace Pb (II) from reclaimed water. *Sep. Purif. Technol.* **2022**, *294*, 121223.
29. Han, X.; Li, G.; Su, W.; Xu, X.; Yu, M.; Wu, G.; Xing, W. Cu-based composite materials derived from MOFs for visible light PMS activation in tetracycline removal. *Colloids Surf. A Physicochem. Eng. Asp.* **2024**, *702*, 135147. [CrossRef]
30. Yuan, D.; Shang, C.; Cui, J.; Zhang, W.; Kou, Y. Removal of Cr (VI) from aqueous solutions via simultaneous reduction and adsorption by modified bimetallic MOF-derived carbon material Cu@ MIL-53 (Fe): Performance, kinetics, and mechanism. *Environ. Res.* **2023**, *216*, 114616. [CrossRef] [PubMed]
31. Moumen, E.; Bazzi, L.; El Hankari, S. Aluminum-fumarate based MOF: A promising environmentally friendly adsorbent for the removal of phosphate. *Process Saf. Environ. Prot.* **2022**, *160*, 502–512. [CrossRef]

32. Zhou, L.; Li, N.; Owens, G.; Chen, Z. Simultaneous removal of mixed contaminants, copper and norfloxacin, from aqueous solution by ZIF-8. *Chem. Eng. J.* **2019**, *362*, 628–637. [CrossRef]
33. Mojtahedi, N.; Zare-Dorabei, R.; Hossein Mosavi, S. A Zn-Based Metal-Organic Framework Modified by $CuCl_2$ Under Ambient Conditions for Simultaneous Ultrasonic-Assisted Removal of Pb and Cd Ions with Fast Kinetics from Aqueous Solution. *Chemistryselect* **2023**, *8*, e202204948. [CrossRef]
34. Li, G.; Ji, G.; Sun, X.; Du, W.; Liu, W.; Wang, S. Layered Metal Organic Framework for Effective Removal of ^{137}Cs from Aqueous Solution. *J. Inorg. Mater* **2019**, *35*, 367–372.
35. Li, M.; Yuan, G.; Zeng, Y.; Peng, H.; Yang, Y.; Liao, J.; Yang, J.; Liu, N. Efficient removal of Co (II) from aqueous solution by flexible metal-organic framework membranes. *J. Mol. Liq.* **2021**, *324*, 114718. [CrossRef]
36. Gu, A.; Chen, K.; Zhou, X.; Gong, C.; Wang, P.; Jiao, Y.; Mao, P.; Chen, K.; Lu, J.; Yang, Y. Trimetallic MOFs-derived Fe-Co-Cu oxycarbide toward peroxymonosulfate activation for efficient trichlorophenol degradation via high-valent metal-oxo species. *Chem. Eng. J.* **2023**, *468*, 143444. [CrossRef]
37. Guo, Z.; Yang, F.; Yang, R.; Sun, L.; Li, Y.; Xu, J. Preparation of novel ZnO-NP@ Zn-MOF-74 composites for simultaneous removal of copper and tetracycline from aqueous solution. *Sep. Purif. Technol.* **2021**, *274*, 118949. [CrossRef]
38. Su, Z.; Deng, Z.; Wang, Y.; Ji, C.; Li, F.; Yang, G.; Huang, L. Effects of the Sr/Ca ratio on the bioremediation of strontium based on microbially-induced carbonate precipitation. *J. Environ. Chem. Eng.* **2023**, *11*, 108990. [CrossRef]
39. Lauchnor, E.G.; Schultz, L.N.; Bugni, S.; Mitchell, A.C.; Cunningham, A.B.; Gerlach, R. Bacterially induced calcium carbonate precipitation and strontium coprecipitation in a porous media flow system. *Environ. Sci. Technol.* **2013**, *47*, 1557–1564. [CrossRef] [PubMed]
40. Li, Z.; Vivas, E.L.; Yang, C.; Suh, Y.J.; Cho, K. Layered potassium calcium phosphate with multiple exchangeable cations for Sr (II) and Co (II) removal from water. *Sep. Purif. Technol.* **2022**, *299*, 121789. [CrossRef]
41. Wang, T.; Wang, S.; Luo, R.; Zhu, C.; Akiyama, T.; Zhang, Z. Microencapsulation of phase change materials with binary cores and calcium carbonate shell for thermal energy storage. *Appl. Energy* **2016**, *171*, 113–119. [CrossRef]
42. Chang, P.-H.; Hsu, H.-P.; Wu, S.-C.; Peng, C.-H. Synthesis and formation mechanism of limestone-derived porous rod hierarchical Ca-based metal–organic framework for efficient CO_2 capture. *Materials* **2020**, *13*, 4297. [CrossRef]
43. Gao, Y.; Yao, L.; Zhang, S.; Yue, Q.; Yin, W. Versatile crosslinking synthesis of an EDTA-modified UiO-66-NH2/cotton fabric composite for simultaneous capture of heavy metals and dyes and efficient degradation of organophosphate. *Environ. Pollut.* **2023**, *316*, 120622. [CrossRef]
44. Huo, J.-b.; Yu, G.; Wang, J. Magnetic zeolitic imidazolate frameworks composite as an efficient adsorbent for arsenic removal from aqueous solution. *J. Hazard. Mater.* **2021**, *412*, 125298. [CrossRef] [PubMed]
45. Mirzaei, K.; Mohammadi, A.; Jafarpour, E. Improved adsorption performance of ZIF-8 towards methylene blue dye by hybridization with nanodiamond. *J. Water Process Eng.* **2022**, *50*, 103254. [CrossRef]
46. Xing, W.; Zhang, D.; Cheng, K.; Han, L.; Wei, M.; Yue, Q.; Huang, Y.; Wu, G. Amorphous Bi-BiOx-inducted directional charges transfer in stalactite-like carbon nitride heterojunction for effective photocatalytic H_2O_2 production. *Sep. Purif. Technol.* **2024**, *359*, 130797. [CrossRef]
47. Xing, W.; Liu, C.; Gao, C.; Jin, X.; Feng, F.; Zhang, X.; Wu, G. Polymeric Carbon Nitride Tubular Sponges with Edge Functionalized Phosphonic Groups for Photocatalysis. *J. Inorg. Organomet. Polym. Mater.* **2024**, *34*, 4632–4641. [CrossRef]
48. Shao, W.; Yu, M.; Xu, X.; Han, X.; Chen, Y.; Han, J.; Wu, G.; Xing, W. Design of a Single-Atom In–N3–S site to Modulate Exciton Behavior in Carbon Nitride for Enhanced Photocatalytic Performance. *Small* **2024**, *20*, 2306567. [CrossRef]
49. Guo, J.; Wang, Z.; Zhang, G.; Liu, S.; Dong, L.; Gu, P.; Hou, L.A. Rapid and effective removal of strontium ions from aqueous solutions by a novel layered metal sulfide NaTS-2. *J. Radioanal. Nucl. Chem.* **2023**, *332*, 2367–2378. [CrossRef]
50. Yao, C.; Dai, Y.; Chang, S.; Zhang, H. Removal of cesium and strontium for radioactive wastewater by Prussian blue nanorods. *Environ. Sci. Pollut. Res.* **2023**, *30*, 36807–36823. [CrossRef] [PubMed]
51. Abass, M.; Abou-Lilah, R.; Abou-Mesalam, M. Selective separation of cobalt ions from some fission products using synthesized inorganic sorbent. *J. Inorg. Organomet. Polym. Mater.* **2024**, *34*, 2176–2189. [CrossRef]
52. Guo, X.; Wang, J. A general kinetic model for adsorption: Theoretical analysis and modeling. *J. Mol. Liq.* **2019**, *288*, 111100. [CrossRef]
53. Rallapalli, P.B.S.; Choi, S.S.; Moradi, H.; Yang, J.-K.; Lee, J.-H.; Ha, J.H. Tris (2-benzimidazolyl) amine (NTB)-modified metal-organic framework: Preparation, characterization, and mercury ion removal studies. *Water* **2023**, *15*, 2559. [CrossRef]
54. Fu, K.; Liu, X.; Lv, C.; Luo, J.; Sun, M.; Luo, S.; Crittenden, J.C. Superselective Hg (II) removal from water using a thiol-laced MOF-based sponge monolith: Performance and mechanism. *Environ. Sci. Technol.* **2022**, *56*, 2677–2688. [CrossRef]
55. Sterba, J.H.; Sperrer, H.; Wallenko, F.; Welch, J.M. Adsorption characteristics of a clinoptilolite-rich zeolite compound for Sr and Cs. *J. Radioanal. Nucl. Chem.* **2018**, *318*, 267–270. [CrossRef] [PubMed]

56. Zhang, Y.-Y.; He, Y.; Zhang, K.-N.; Chen, Y.-G.; Ye, W.-M. Montmorillonite alteration and its influence on Sr (II) adsorption on GMZ bentonite. *Environ. Earth Sci.* **2021**, *80*, 791. [CrossRef]
57. Choi, S.; Kim, B.-J.; Seo, S.; Lee, J.-K.; Kwon, J.-S. Characterization of the Purified Ca-type Bentonil-WRK Montmorillonite and Its Sorption Thermodynamics With Cs (I) and Sr (II). *J. Radioact. Waste Soc.* **2023**, *21*, 427–438. [CrossRef]